Materials & Design 263 (2026) 115629



Contents lists available at ScienceDirect

Materials & Design

journal homepage: www.elsevier.com/locate/matdes



On the origin of spontaneous electrical oscillations in a minimal peptide assembly

Salvatore Del Basso [a], Pietro Squeri [a], Rishit Mohan Ahuja [b], Rishav Karki [b], Giuseppe De Giorgio [a], Vardan Galstyan [a], Raffaele Martucci Zecca [c], Enrico Dalcanale [c], Xiongchuan Huang [d], Davide Vurro [a], Saksham Sharma [e], Pasquale D'Angelo [a,*], Andrew Adamatzky [f], Giuseppe Tarabella [a,f]

[a] Institute of Materials for Electronics and Magnetism (IMEM) - National Research Council of ItalyItaly (CNR), Parco Area delle Scienze 37A, 43124 Parma, Italy
[b] Mathematics and Archives Centre, Homerton Street, University of Cambridge, Cambridgeshire CB2 0NT, UK
[c] Department of Chemistry, Life Sciences and Environmental Sustainability, University of Parma (Italy), Parco Area delle Scienze 17/A, 43124 Parma, Italy
[d] School of Information Science and Technology, Fudan University, Handan Rd.2020, Shanghai, China
[e] Cambridge Centre for Physical Biology (CCPB), University of Cambridge, Wilberforce Road, CB30WA Cambridgeshire, UK
[f] Unconventional Computing Laboratory, University of the West of England, Bristol BS16 1QY, UK

A B S T R A C T

The design of functional materials involves understanding how complex functionalities can emerge from simple material building blocks. In this context, peptide-based systems represent a versatile materials platform due to their chemical diversity, tunability and compatibility with sustainable processing routes. However, the conditions under which electrical functionality can emerge in minimal, abiotic peptide assemblies remain poorly understood. Here, we report the design and characterization of a minimal peptide-based material obtained through abiotic thermal polymerization, exhibiting spontaneous and persistent electrical oscillations under constant environmental conditions. The material is formed by the thermal condensation of four amino acids (Asp, Glu, Arg, Leu), resulting in a chemically heterogeneous ensemble of short oligomeric peptides. A comprehensive materials characterization combining DOSY NMR, HPLC-MS, FTIR, DLS, SEM, and qualitative Biuret assays reveals a disordered, proteinoid-like assembly with dynamic aggregation–disaggregation behaviour and strong coupling to ionic transport in the surrounding medium. Electrical measurements demonstrate autonomous oscillatory signals arising under constant environmental conditions and in the absence of external stimulation. Simultaneous dynamic light scattering and electrical measurements reveal a direct correlation between electrical oscillations and aggregation–disaggregation dynamics, indicating that the electrical activity emerges as a collective property of chemically heterogeneous peptide ensembles rather than from individual molecular species. These results provide experimentally grounded insight relevant to the design of peptide-based functional materials, highlighting minimal peptide assemblies as a promising platform for adaptive sensing, bio-inspired interfaces, and unconventional computing applications.

1. Introduction

Peptides, both natural and synthetic, are promising materials for a range of technological applications, particularly in the field of peptide electronics, due to their unique self-assembling properties and functional versatility. In Nature, peptides are fundamental building blocks of proteins, playing essential structural and biological roles. Synthetic peptides are studied to shed light on prebiotic processes related to the origin of life, particularly the formation of early protein-like structures [1]. Recently, their scope of application has significantly expanded: several studies demonstrate the potential of peptide-based systems as building blocks for material-based information processing, particularly within Unconventional Computing (UC) paradigms [2–5].

Research in the emerging field of *peptide electronics* has highlighted the semiconducting behaviour of certain peptide assemblies [6]. Additionally, although still limited in number, some examples of peptide-based biosensors have been reported, including electrochemical sensors [7], and target-related sensors for disease biomarker detection [8]. Historically, the concept of using minimal peptides, also referred in literature as proteinoids, or thermal proteins, has its roots in early work by Sidney W. Fox, who first demonstrated that such structures could exhibit membrane-like properties and excitability reminiscent of primitive cellular behaviour [9–11].

These observations, originally framed in the context of origin-of-life studies, laid the groundwork for considering proteinoids as dynamic systems capable of information processing. More recently, in the

* Corresponding author.
E-mail address: pasquale.dangelo@cnr.it (P. D'Angelo).

https://doi.org/10.1016/j.matdes.2026.115629
Received 3 September 2025; Received in revised form 4 February 2026; Accepted 6 February 2026
Available online 7 February 2026
0264-1275/© 2026 The Author(s). Published by Elsevier Ltd. This is an open access article under the CC BY license (http://creativecommons.org/licenses/by/4.0/).

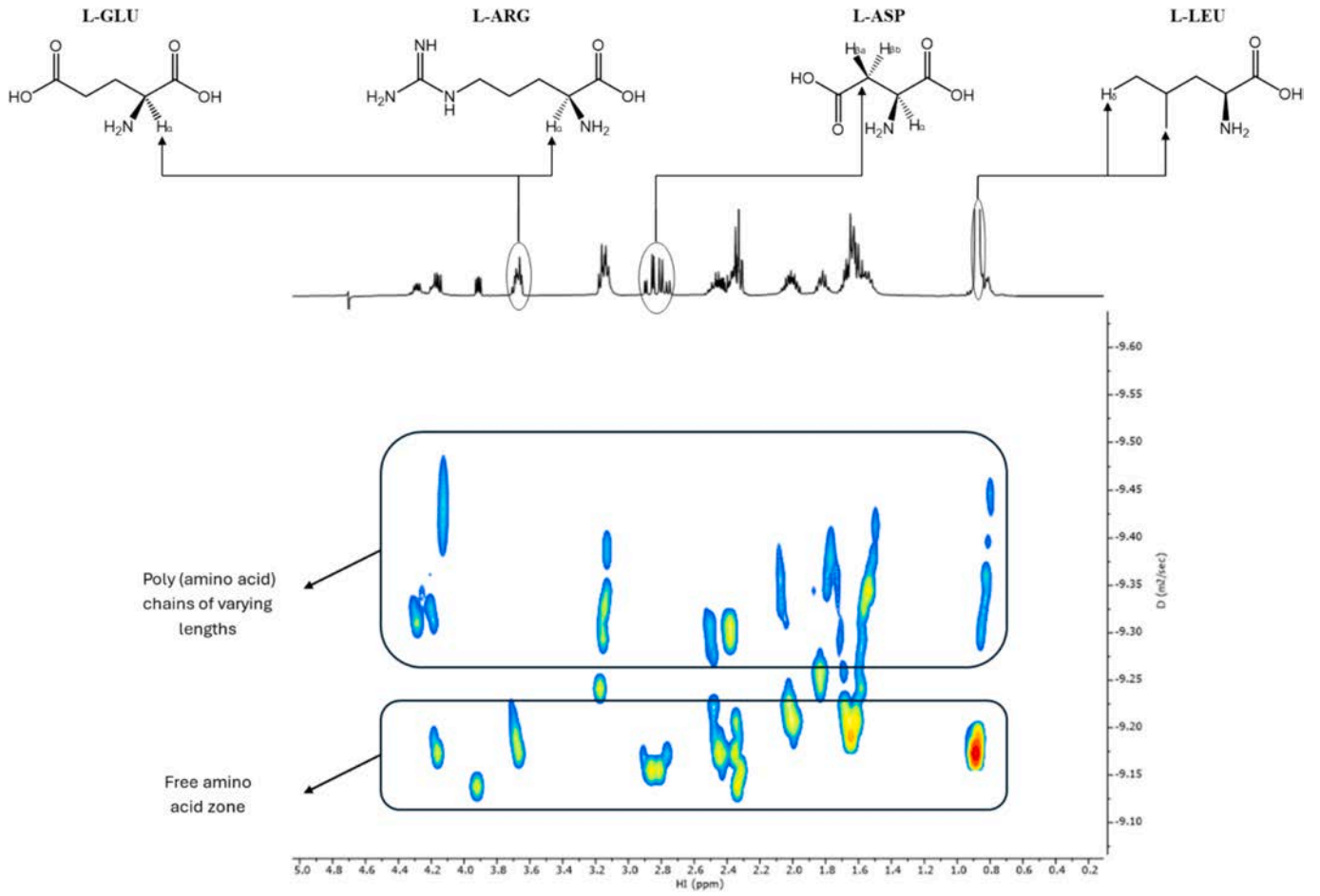


Fig. 1. The chemical structures of the amino acid residues constituting the investigated peptide: L-aspartic acid (L-Asp), L-leucine (L-Leu), L-arginine (L-Arg), and L-glutamic acid (L-Glu) and the DOSY NMR of the protenoid in D_2O at 400 MHz.

framework of unconventional computing, A. Adamatzky has revisited proteinoids from a computational perspective, exploring their electrical activity and responsiveness [12,13]. In this framework, proteinoids active matter capable of supporting spatiotemporal signal propagation, memory effects, and basic logic operations, offering a radically different approach to computation rooted in biochemistry and self-organization.

Despite some results in literature disclosing several features of proteinoids, such as optical responsiveness or oscillatory signals, a comprehensive discussion of the mechanisms underlying the phenomenology of such signals, is still lacking.

Recent advances in peptide nanoarchitecture have further expanded the spectrum of structural states accessible to minimal peptide systems. In particular, several studies have shown that amino acids and short peptides can give rise to noncovalent peptide glasses when subjected to controlled heating–quenching processes [14,15]. These biomolecular glasses represent a distinct amorphous state stabilized by dense networks of weak intermolecular interactions, exhibiting optical, mechanical and dynamic features that differ markedly from classical crystalline or fibrillar assemblies. Their emergence highlights how even simple peptide building blocks can access complex free-energy landscapes, generating metastable, non-equilibrium states with collective properties. This recent development further strengthens the idea that peptide-based systems are capable of supporting diverse forms of emergent behaviour, providing an additional conceptual framework for interpreting the dynamic electrical phenomena investigated in this work.

A theoretical framework for the origin of such electrical excitability was proposed by Matsuno in 1984, who suggested that the dynamic interaction between basic and acidic proteinoids, governed by material flow equilibration, could lead to intrinsic electrical spiking in proteinoid microspheres [16].

Our results, based on minimal peptide assemblies, provide experimental support for this early model, suggesting that similar mechanisms may still operate in abiotic systems. Within this framework, the present work investigates a minimal peptide-based material obtained through abiotic, non-enzymatic thermal polymerization of four amino acids (L-aspartic acid, L-glutamic acid, L-arginine, and L-leucine), with the aim of elucidating the material-level origin of the spontaneous oscillatory electrical behaviour observed in such systems. The study does not target a predefined electrical response, but rather seeks to understand how collective electrical activity can emerge from chemically heterogeneous minimal peptide assemblies formed through simple abiotic processing routes. The system is first characterized using complementary spectroscopic and morphological techniques, including FTIR spectroscopy, SEM imaging, and dynamic light scattering, to assess its chemical composition, structural features, and aggregation behaviour in aqueous environments. A dedicated experimental setup is then employed to probe the electrical response of the material under constant environmental conditions. Crucially, electrical signals are recorded simultaneously with *operando* Dynamic Light Scattering (DLS) measurements, in support of the hypothesis that the electrical behaviour of MPA is linked to a dynamic aggregation/disaggregation process, as originally proposed by Matsuno in 1984 [16], and further developed in 2024 [17]. This combined experimental approach provides a materials-level basis for interpreting the observed electrical activity as an emergent collective property of the peptide assembly. By establishing a direct link between aggregation–disaggregation behaviour and electrical oscillations, the

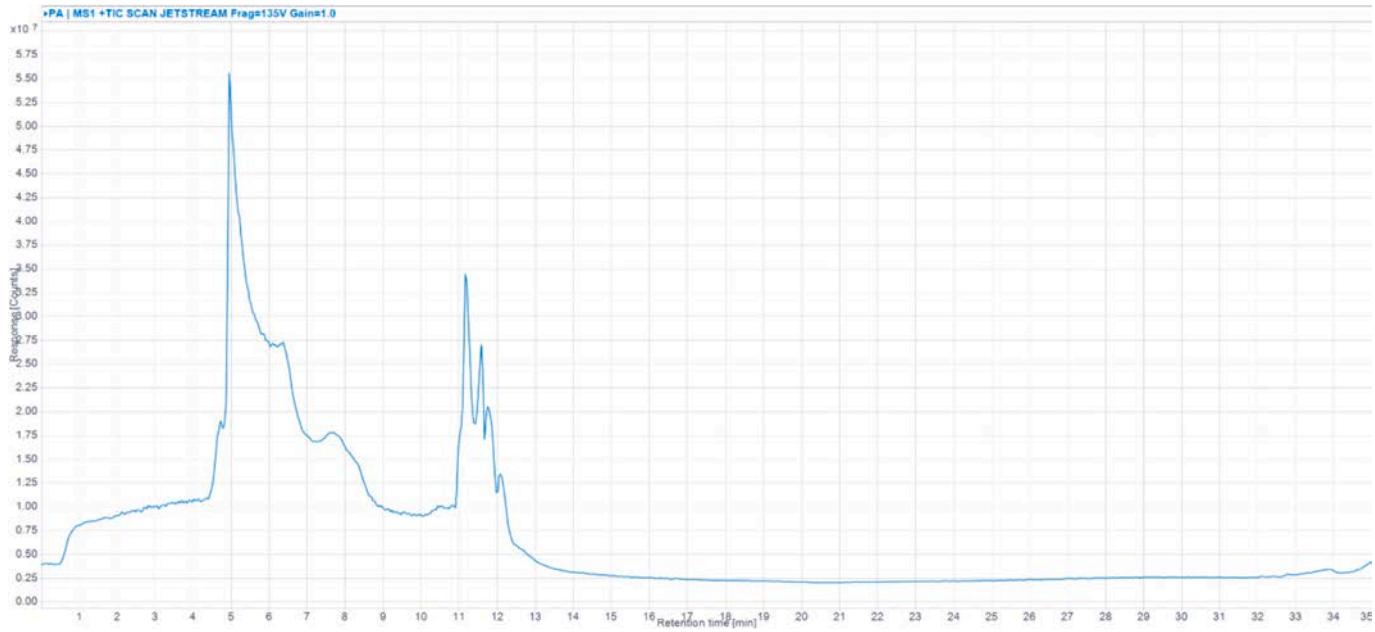


Fig. 2. HPLC-MS chromatogram.

present study contributes to bridging concepts from prebiotic chemistry and contemporary peptide-based materials research, and highlights the potential of minimal peptide assemblies as functional materials for peptide electronics and unconventional computing architectures.

2. Results and discussion

2.1. Peptide powder synthesis and characterization

A MPA composed of four amino acid units (L-aspartic acid, L-glutamic acid, L-arginine, and L-leucine) was synthesized by thermal polymerization, following a protocol used for the synthesis of thermal proteins [12]. Specifically, amino acids were mixed in a weight ratio of (1:1:1:1) to obtain a homogeneous powder. The mixture was transferred into a round-bottom three-neck flask equipped with a nitrogen inlet, heated at 150–160 °C under N_2 atmosphere for 4.5 h with a ramp of approximately 5 °C min^{-1}, and stirred mechanically to ensure uniform melting, condensation and an anhydrous environment. During heating, the amino acids underwent dehydration and condensation to form peptide bonds, yielding a viscous melt that progressively darkened in colour. Then, the reaction mixture was allowed to cool naturally to room temperature, after which it solidified. The resulting polymer material was pulverized and washed with deionized water to remove unreacted monomers and then lyophilized to obtain a dry powder. The resulting powder was a brownish glassy solid. After lyophilization, the MPA powder was diluted in water to a concentration of 10 mg/mL and sonicated before optical and morphological characterization to make a uniformly distributed and homogeneous dispersion of MPA. These components were selected to provide a balanced combination of charged and hydrophobic moieties, enabling the interplay between electrostatic and hydrophobic interactions that determine both aggregation behaviour and electrical activity.

The peptide assembly is obtained by melt oligomerization of the mix of four amino acids. The amino acids distribution in the products is random. We tested several techniques to determine the product distribution in terms of type and length of the oligomers. The most reliable results were obtained using DOSY NMR.

DOSY NMR uses pulsed field gradients to differentiate molecular species based on their diffusion coefficient, D along the z axis. The D value is inversely related to the hydrodynamic radius of the species: smaller molecules (unreacted amino acids) have high D values and are located in the low part of the plot, while larger species (protenoids) show low D values and are located in the higher part. In the DOSY spectrum, the X-axis report the chemical shifts in ppm, while the Y-axis represent the diffusion coefficient D in a logarithmic scale. In this way we were able to show that the final proteinoid is a mixture of short polymeric species together with some residual unreacted amino acids. The main information that can be deduced from the DOSY analysis highlighted in Fig. 1, is the following:

- **Aspartic Acid (Asp):** The signals attributed to the protons H_α 3.93–3.90 ppm, $H_{\beta a}$ and $H_{\beta b}$ 2.86–2.79 ppm are exclusively found in the high-diffusion region. This observation is consistent with the presence of unreacted aspartic acid. The absence of Asp signals at low D values suggests that aspartic acid may not have been significantly incorporated into the protenoid structure.
- **Leucine (Leu)**: The identifying signal of the H_δ protons of leucine is observed as a system of peaks in the high-diffusion region (0.89–0.86 ppm), indicating the presence of an unreacted leucine fraction. However, unlike aspartate, an additional signal system is present at 0.82–0.81 ppm. Its location in the low-diffusion region confirms the presence of a leucine moiety in the protenoid chain.
- **Arginine (Arg) and Glutamic Acid (Glu)**: The H_α proton signals of Arginine 1 and Glutamic Acid 1, with chemical shifts between 4.29–4.27 ppm and 4.18–4.16 ppm, are characterized by low diffusion coefficients. This finding implies the presence of both amino acids within the polymer chains.
- **Free Fraction of Arg and Glu**: In contrast, a second set of H_α signals attributable to Arginine 2 and Glutamic Acid 2 was detected at 3.68–3.66 ppm. The association of these signals with high diffusion coefficients is indicative of the free amino acid fraction.

The attribution of all NMR signals has been done using 2D-TOCSY and 2D-HSQC spectroscopy.

To further elucidate the molecular complexity of the thermally polymerized peptide ensemble, and to complement the information obtained from DOSY NMR, HPLC–MS analysis was performed. This technique provides an independent assessment of molecular weight distribution and chemical heterogeneity, allowing the presence of oligomeric peptide species with different chain lengths and polarities to be

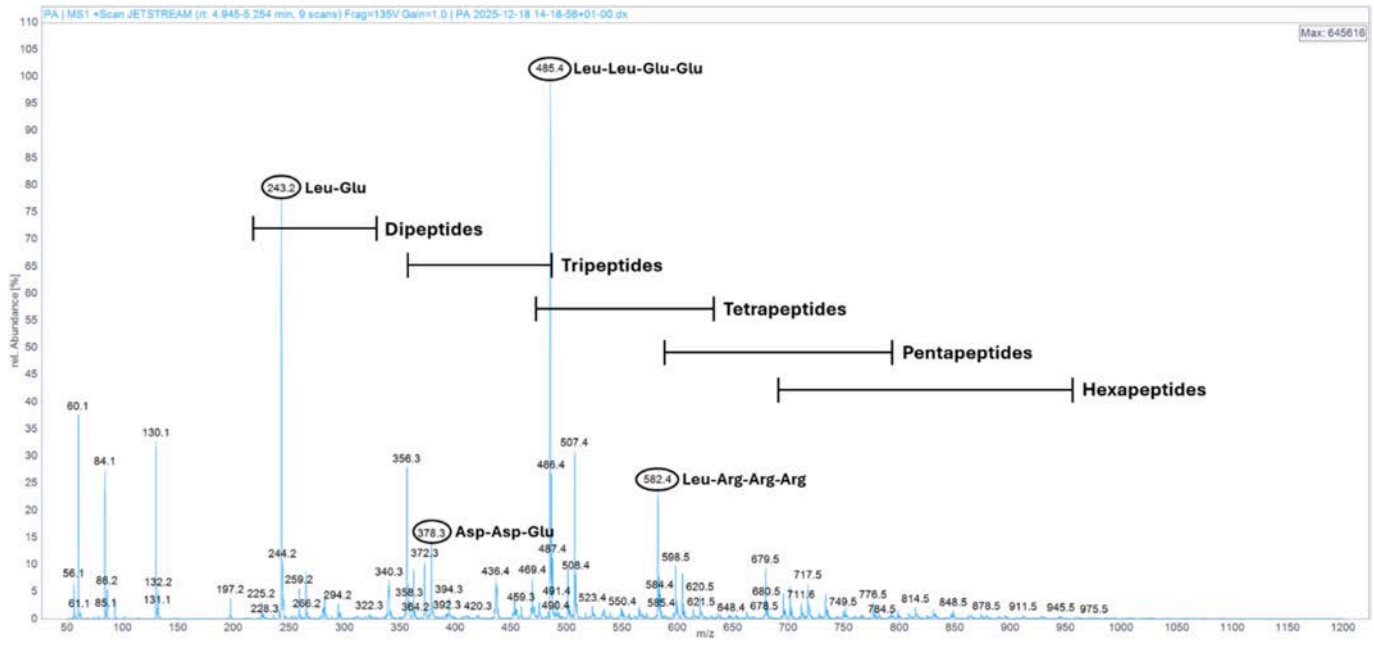


Fig. 3. 4,9–5,2 min peak mass spectra.

directly probed. The following HPLC–MS results therefore serve to characterize the ensemble nature of the system, rather than to resolve individual peptide sequences or quantify specific components.

The HPLC-MS analysis was performed using a cyano (CN) bonded stationary phase. The mobile phase consisted of (A) acetonitrile and (B) water, both acidified with 0.05% trifluoroacetic acid (TFA). A linear gradient from 100% A to 100% B was applied. The resulting chromatogram (Fig. 2) exhibits a broad signal between 4.9 and 6.5 min, partially co-eluting with the solvent front, followed by a tailing edge (7–9 min) and four distinct, though partially overlapping, peaks between 11 and 13 min. Mass spectrometry (ESI+) confirmed that the early-eluting fractions correspond to the most hydrophobic species, with *m/z* values ranging from 197.2 to 751.5.

Given the stochastic nature of the reaction, the product mixture contains a statistical distribution of peptides. Based on the observed molecular weights, these species range from dipeptides to hexapeptides. Specifically:

- **Dipeptides:** *m/z* 226–330 (including cyclic forms);
- **Tripeptides:** *m/z* 356–486;
- **Tetrapeptides:** *m/z* 470–642;
- **Pentapeptides:** *m/z* 587–799;
- **Hexapeptides** *m/z* 697–955.

In regions of mass overlap, unambiguous chain length assignment was not possible. However, the peak at *m/z* 243.2 is consistent with the $[M + H]^+$ ion of the cyclic Leu-Glu dipeptide (calculated 243.1 Da). Its early elution is consistent with the high hydrophobicity of the leucine

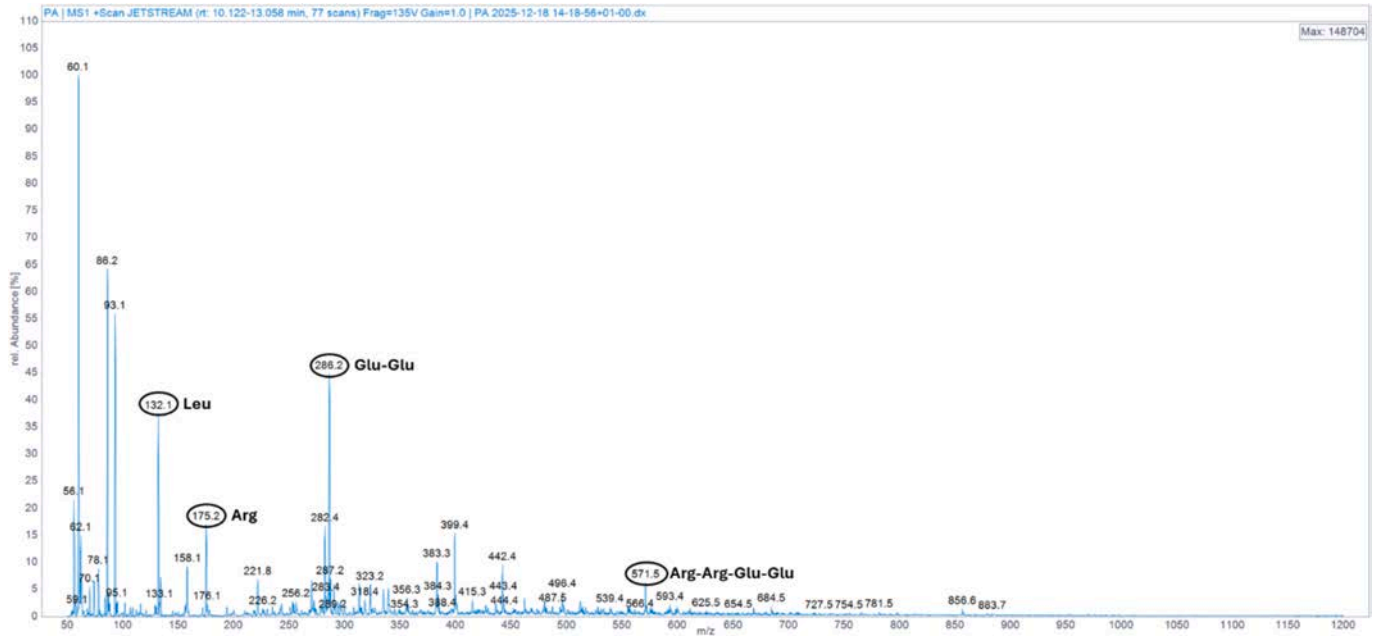


Fig. 4. 10,1–13,1 min peak mass spectra.

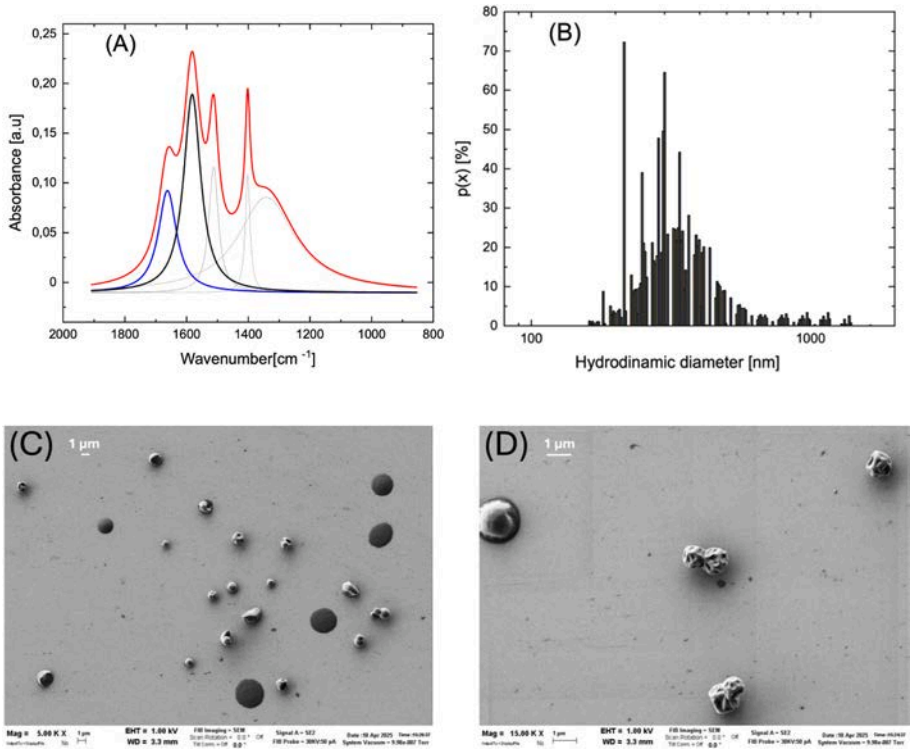


Fig. 5. (A) FTIR analysis. Deconvoluted peaks indicates the presence of amide I and II bands in 1660 cm^{-1} (blue curve) and 1580 cm^{-1} (black curve) respectively. (B) size distribution from DLS. (C) SEM shows smooth, compact morphology consistent with proteinoid-like aggregations, in the magnified image (D) Magnified SEM image highlighting associated peptide spherules; these observations are consistent with the hypothesis that aggregation–disaggregation dynamics play a role in the observed electrical behaviour. [18,19]. (For interpretation of the references to colour in this figure legend, the reader is referred to the web version of this article.)

side chain. Furthermore, additional signals such as *m/z* 378.3 are consistent with the linear tripeptide Asp-Asp-Glu (calculated 378.1 Da). Similarly, the signal at *m/z* 485.4 is consistent with the cyclic form of the tetrapeptide Leu-Leu-Glu-Glu (calculated 485.2 Da), while the peak at *m/z* 582.4 can be assigned to the cyclic form of the tetrapeptide Leu-Arg-Arg-Arg (calculated 582.4 Da), further supporting the occurrence of head-to-tail cyclization during synthesis. Heavier species at *m/z* 679.5 and 715.5 may be attributed to either penta- or hexapeptides (Fig. 3).

In the peaks between 11 and 13 min, we can detect the presence of unreacted arginine and leucine. The higher retention is consistent with the higher polarity of the gradient conditions. Notably, the signal at *m/z* 442.4 likely represents a tripeptide, while the *m/z* 286.2 fragment could stem from in-source fragmentation (loss of an arginine residue without a water molecule 156 Da). Furthermore, *m/z* 286.2 likely corresponds to a cyclic Glu-Glu dipeptide $[M + H]^+$. Within this retention window, a signal at *m/z* 571.5 was also observed, which is consistent with the cyclic form of the tetrapeptide Arg-Arg-Glu-Glu (calculated 571.3 Da) (Fig. 4).

In conclusion, HPLC-MS analysis confirms the formation of a complex mixture comprising unreacted monomers and oligomers (2 to 6 residues) linear and cyclic. Hydrophobic fractions are enriched in leucine, whereas polar fractions predominantly contain arginine and glutamic acid-based species. The relative abundance of these species cannot be quantitatively determined from the current data.

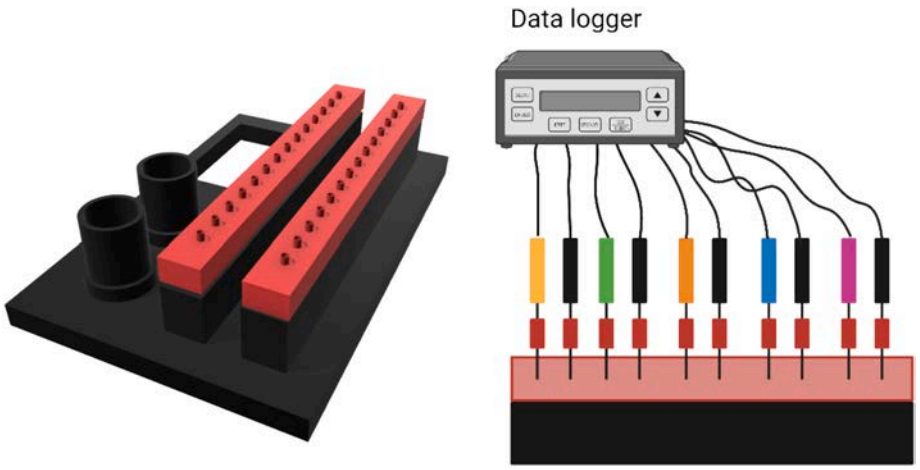


Fig. 6. (A) Rendering of the 3D-printed support hosting the electrodes immersed in the MPA dispersion; (B) Colour schematics of the series of electrodes connected to the DAQ data logger. Created in BioRender. Del Basso S., G. (2025) https://BioRender.com/yus1p84.

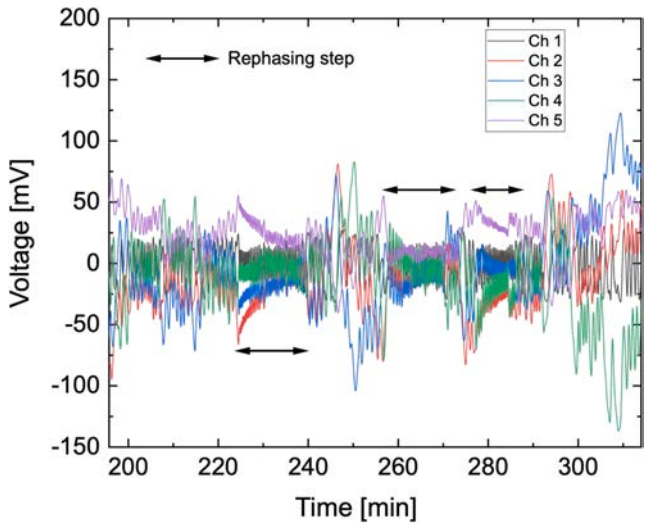


Fig. 7. *Voltage* vs *time* plot of the signals acquired by 5 electrodes immersed in the MPA aqueous dispersion. The arrows indicate the time interval in which a kind of synchronization of electrical signals from the electrodes rephase.

2.2. Characterization

Fourier-transform infrared spectroscopy (FTIR) was used to verify the success of the thermal synthesis of amino acids, as well as to analyse the molecular structure and chemical bonding within the peptide assemblies. The FTIR spectrum exhibited characteristic amide I and II bands at 1660 cm^{-1} and 1580 cm^{-1}, respectively, confirming the presence of peptide bonds (Fig. 5A). These results confirm the synthesis of the peptide and provide insights into the interactions driving its self-assembly. A qualitative Biuret assay further confirmed the presence of peptide bonds in the thermally polymerized material. DLS was employed to analyse the size distribution of peptides in the aqueous dispersion. DLS data showed a main population of particles with an average hydrodynamic diameter of 500 nm, as well as a smaller population of larger aggregates around 1000 nm in size (Fig. 5B). This suggests the formation of stable aggregates in the dispersion.

SEM micrographs showed the presence of sub-micron-sized aggregates with spherical shape (Fig. 5C**),** indicating a tendency for the peptide to form higher-order structures through self-assembly and compact morphology, as already observed in literature, [13] with surface features hinting at dynamic fusion or growth processes. The results suggest the presence of interacting peptide aggregates within a heterogeneous population, supporting the hypothesis that aggregation–disaggregation dynamics are directly coupled with the electrical signals. This interplay indicates that the electrical response may reflect, in real time, the structural reorganization occurring within the system. The SEM image is consistent with the size range observed by DLS, falling approximately in the range of 500–1000 nm.

3. Electrical oscillations: Acquisition and analysis

The electrical properties of MPA were investigated using a Keithley DAQ 6510 data acquisition system in DC voltage mode at 1 Hz sampling. Five channels were connected to the peptide aqueous dispersion, while an additional channel, serving as a reference, was connected to an aqueous dispersion acting as the blank, as shown in Fig. 6B. Prior to measurements, all electrodes were sterilized and carefully immersed in the peptide dispersion. The setup was placed inside a biological safety cabinet to ensure consistent and contamination-free conditions.

A custom 3D-printed PLA support was designed and printed (Fig. 6A) to host the electrodes immersed in the MPA dispersion. The support serves to lodge 5 couples of electrodes ensuring a stable experimental setup to minimize instrumental and environmental errors and to preform replicates. Specifically, the distance between each pair of electrodes was fixed at 0.5 cm. This as-fabricated measurement setup also protected the MPA dispersion from external environment. The setup allows for the 5/pairs electrodes to be exposed to the same dispersions and capture collective behaviour of the MPA. Data has been recorded starting from a few hours to 24 h-lasting measurement runs, sampled at 1 Hz; the long-term acquisition allowed for the identification of transient and stable electrical signals.

Fig. 7 shows the electrical signals representing the spontaneous oscillatory behaviour with a characteristic synchronous/asynchronous dynamic. The oscillations exhibited well-defined patterns that repeat over time. During a synchronous step, the voltage across multiple channels (from Ch 1 to Ch 5) displayed synchronized fluctuations, with amplitudes ranging from −150 to +150 mV over a period from 20 to 30 min. This suggests a collective behaviour of the peptide assemblies, potentially driven by the movement of charged amino acid residues and aggregation effects [16].

Fig. 8 shows a zoom-in view of a detailed 15-minute window (interval from 220 to 245 min), where the voltage oscillations showed a consistent pattern with amplitudes varying between −50 and +200 mV. This stability over short time scales further confirms the robustness of the electrical activity. The overall period of oscillation falls in the range of about 20 s, while the voltage fluctuations were observed with a smaller amplitude of approximately 0.66 mV, indicating the presence of both high- and low-amplitude oscillatory modes.

The synchronized oscillations observed across multiple channels suggest that the peptide assemblies exhibit a form of collective activity, which may arise from cooperative interactions between individual peptide residues. This collective behaviour is supported by a synchronous/asynchronous dynamic. The reference channel connected to blank served as a control (SI): in contrast to the peptide aqueous dispersion, the water-only dispersion did not exhibit comparable electrical

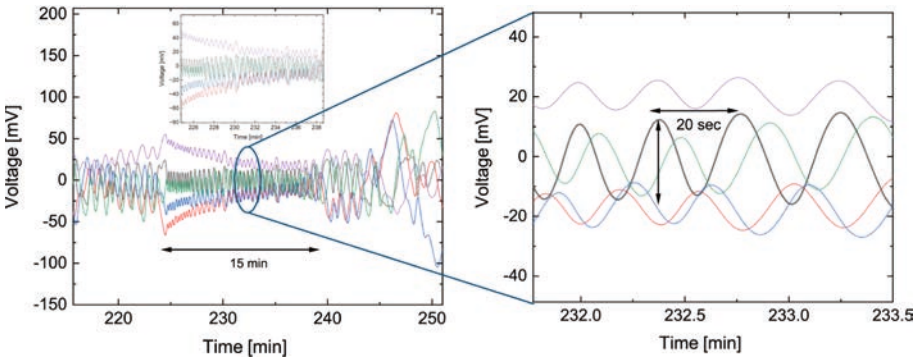


Fig. 8. (Left) A magnification along the timescale of synchronized oscillations of the 5-channel MPA electrodes, the inset showing a zoom of the 15 min window; (Right) Zoom of the period and amplitude of the single oscillatory waves.

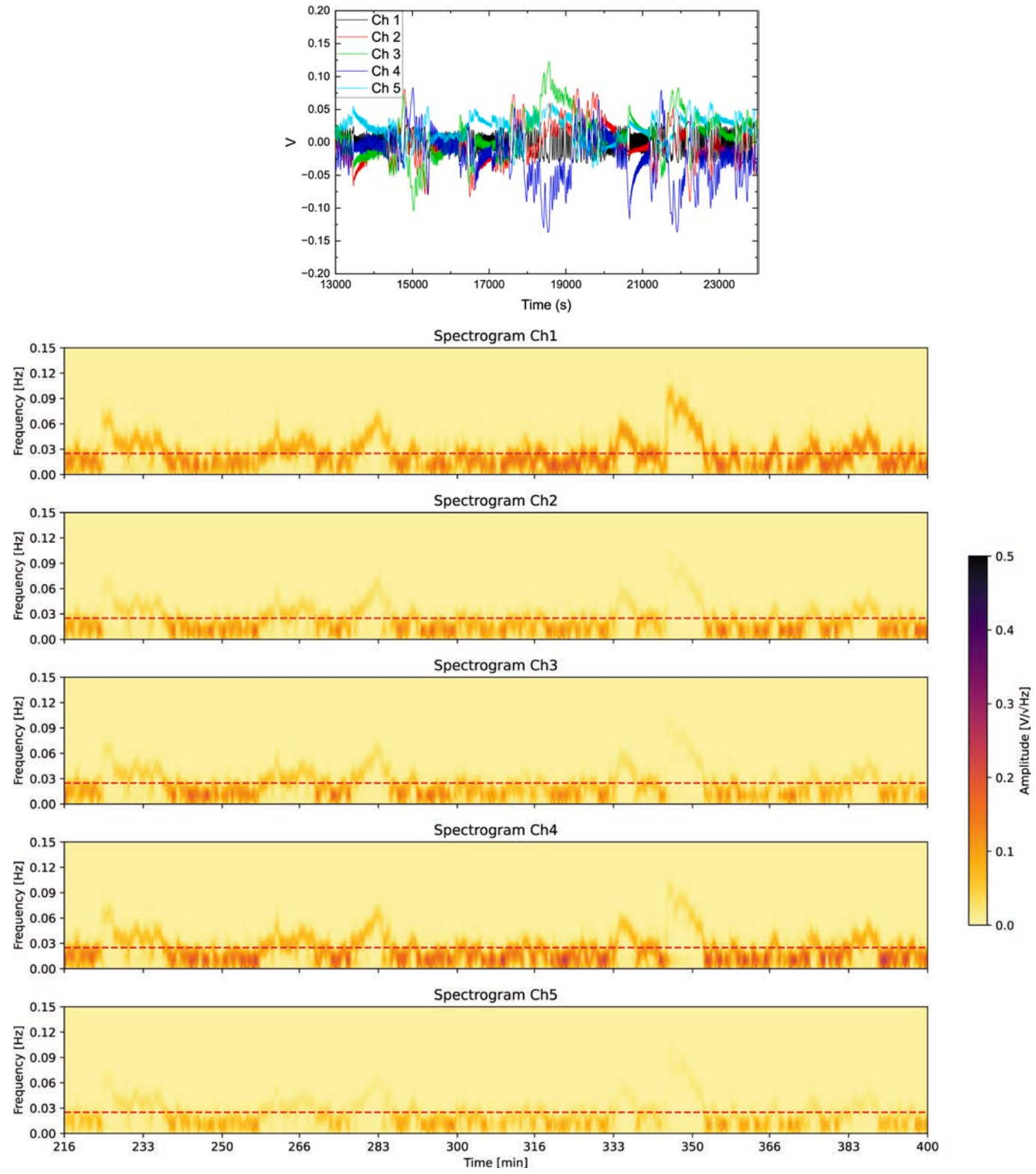


Fig. 9. (A) Zoom on the 216–400 min time window of the voltage signals recorded by the 5 electrodes in the MPA dispersion. (B) Spectrogram computed from the same interval; each horizontal stack in the plot represents one electrode channel, arranged from top (channel 1) to bottom (channel 5). The red dashed lines indicate the threshold frequency of 0.025 Hz, above which synchronous behaviour becomes evident, as discussed in the main text. Notably, the regions that appear more uniform across the five channels in panel (A) (e.g., around 233, 283, and 350 min) correspond to higher-frequency components in the spectrogram. (For interpretation of the references to colour in this figure legend, the reader is referred to the web version of this article.)

behaviour, showing only minor noise fluctuations and no significant oscillatory activity. This confirms that the observed electrical behaviour is characteristic of the peptide assemblies.

To identify recurring patterns over time, quantitative parameters describing the synchronous and asynchronous oscillations were extracted. To analyse the time-varying spectral structure of five simultaneously acquired signals, a *spectrogram* was calculated for each channel over a common time interval. The data were processed using the Python NumPy, [20] SciPy [10], and Matplotlib libraries. [21] Since each row of the original dataset included an explicit timestamp in the first column (followed by five voltage signals), the sampling rate was not assumed as fixed but was instead estimated as the inverse of the mean time difference between consecutive timestamps. This approach compensates for small acquisition irregularities (such as jitter, rounding or numerical imprecision), and provides a more accurate and robust estimate of the actual sampling frequency compared to assuming a constant interval. Each signal was divided into 100-sec time windows with a 75% overlap between consecutive windows. To reduce spectral leakage, each window was modulated using a Hann window. A short-time Fourier transform (STFT) was applied to each window, with 1024 FFT points. The result is a matrix Sxx(f,t) containing the power spectral density (PSD) for each frequency-time pair, which was subsequently transformed into an amplitude spectral density. To attenuate possible 50 Hz interference, an optional notch filter was applied. The filter is implemented using an IIR structure centered at 50 Hz, with a quality factor Q = 30, and applied in zero-phase mode using the 'filtfilt' method (to avoid phase distortion) [22]. In the specific case under analysis, no dominant spurious components at 50 Hz were observed.

Fig. 9 illustrates a representative 216–400 min time window of the voltage signals recorded by the five electrodes in the MPA dispersion and the corresponding spectrogram. Each horizontal band in panel B represents one electrode channel, arranged from top (channel 1) to bottom (channel 5). Regions appearing more uniform across the five channels in panel A (e.g., around 233, 283, and 350 min) correspond to higher-frequency components in the spectrogram, as shown in panel B. The dotted red line in the spectrogram marks the threshold frequency of 0.025 Hz, above which synchronous behaviour becomes evident. Above this threshold, channels display correlated oscillatory patterns indicative of network-level synchronicity.

This analysis aimed to identify and characterize periods of synchronicity in multichannel signals recorded across five channels, employing automated Python scripts specifically developed for this purpose. Synchronicity was interpreted in relative terms, not as exact signal matching, but rather as a concordance in amplitude and frequency patterns across channels [19]. To achieve a robust and reliable characterization of the signals' temporal dynamics, a sliding window approach was employed. This method was favoured over direct peak detection on the raw signal, as the latter struggled with consistent peak identification criteria across the extensive recording duration (exceeding 1160 min).

Frequency was calculated as the fundamental oscillation frequency in Hz by detecting peaks within each 30-second window using the scipy.signal.find_peaks function and computing the inverse of the mean inter-peak interval. This approach provided a physically meaningful measure of oscillation frequency, overcoming limitations of simple peak counting methods when dealing with variable waveforms.

The signal was divided into consecutive 30-second windows, and a local analysis was performed on each window. For every window: (1) Amplitude was calculated as the difference between the maximum and minimum values for each channel; (2) Frequency was computed as the fundamental frequency in Hz based on inter-peak intervals. All pairwise combinations between channels (10 in total) were considered. A window was labelled as synchronous if at least 7 out of 10 combinations met both of the following conditions: Difference in amplitude $\leq$0.018 V; Difference in frequency $\leq$0.5 Hz.

This specific threshold of 7 pairs was chosen based on a simple combinatorial rule to guarantee robust network-wide synchrony. It is mathematically possible to have up to 6 synchronized pairs without any group of three channels being all mutually synchronized (for example, if two channels are synchronized with three others, but those three are not synchronized with each other). The addition of a 7th synchronized pair makes this configuration impossible. Therefore, 7 pairs directly ensures that at least one core group of three channels exists where every channel is synchronized with every other, representing a fundamental shift from isolated pairs to a coherent network state. Furthermore, the requirement for 7 pairs derives from Turán's theorem, which states that the maximum number of edges in a graph of 5 nodes without a triangle (a clique K_3) is 6. Therefore, with 7 edges, it is mathematically guaranteed that the graph must contain at least one triangle. This approach, related to the Ramsey number R(3,3), ensures that the identified synchronous state represents a core of robust, highly connected coordination—specifically, a group of at least three channels all mutually synchronized with each other—and not just sparse agreement between isolated pairs.

Table 1
Summary statistics of synchronous and non-synchronous segments over the 83–1167 mins time interval. Segments are defined by grouping at least 4 consecutive time windows with the same synchrony state. The table reports mean duration, number of segments, and signal amplitude and frequency characteristics for synchronous and non-synchronous periods. The standard deviations (STD) represent different types of variability: the duration STD reflects how segment lengths vary; the STD of mean amplitudes indicates variability in average amplitudes across segments; the mean of amplitude STDs quantifies the average amplitude fluctuations within each segment, while the STD of amplitude STDs shows how these within-segment fluctuations vary between segments. Frequency STD describes the variability of mean frequencies across segments. The average number of windows per segment gives an idea of segment length in terms of consecutive windows.

Variable	Synchronous (n = 71)	Non-Synchronous (n = 72)	p-value
Duration (s)			**0.007**
· Mean ± 95% CI	281.7 ± 68.0	164.8 ± 14.8	
· Median (IQR)	179.0 (119.0–269.0)	149.0 (119.0–179.0)	
Amplitude (V)	0.0220 ± 0.0011	0.0269 ± 0.0007	**<0.001**
Frequency (Hz)	0.0103 ± 0.0037	0.0047 ± 0.0023	**0.005**
Windows per segment	9.4	5.5	–

Statistical analysis revealed robust differences between synchronous and non-synchronous segments (Table 1). Duration data exhibited strong positive skewness (Shapiro-Wilk $p < 0.001$ for both groups; standard deviations approximating means), necessitating the use of median and interquartile range (IQR) for robust comparison. Synchronous segments showed significantly longer duration (Mann-Whitney $U = 3229$, $p = 0.007$) with median values of 179.0 s (IQR: 119.0–269.0 s) compared to 149.0 s (IQR: 119.0–179.0 s) for non-synchronous segments, representing a 70.9% increase in mean duration. The substantial discrepancy between mean (281.7 s) and median values for synchronous segments reflects high variability, with most events lasting 2–4.5 min but a few being substantially longer. This pattern, characterized by the identical 25th percentiles but substantially higher 75th percentile for synchronous periods, suggests that these states are not uniformly longer but can occasionally enter particularly stable, long-lasting configurations.

Synchronous segments also exhibited significantly different signal characteristics, with lower mean amplitude (0.0220 ± 0.0011 V vs 0.0269 ± 0.0007 V; Welch's $t(121) = -7.53$, $p < 0.001$) but higher mean frequency (0.0103 ± 0.0037 Hz vs 0.0047 ± 0.0023 Hz; Mann-Whitney $U = 3188$, $p = 0.005$). The 118.3% increase in frequency and 18.4% decrease in amplitude during synchronous periods were both statistically significant.

As shown in Figs. 6 and 7, segments classified as synchronous systematically aligned with regions of higher-frequency activity, visually

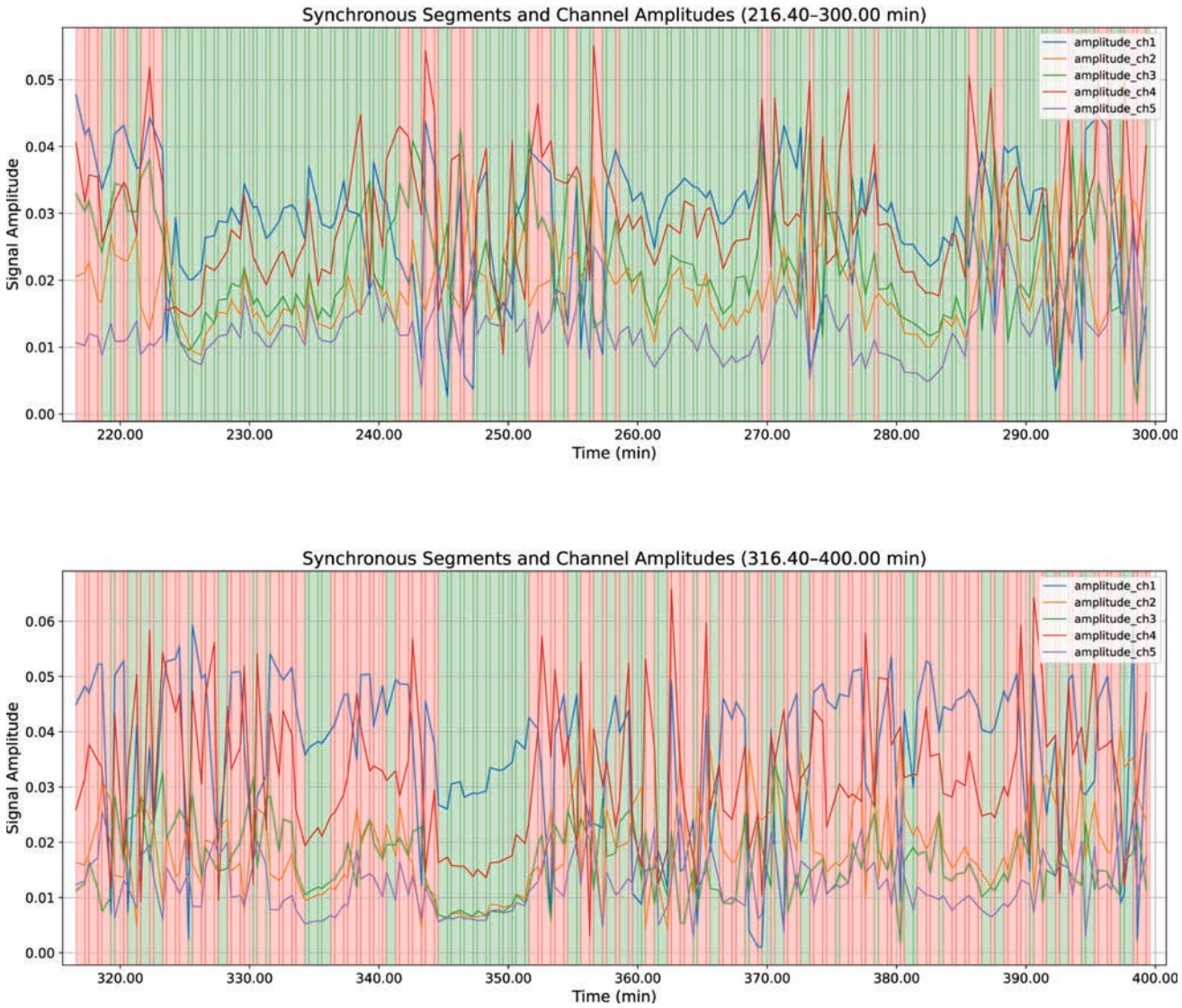


Fig. 10. Visualization of channel amplitudes and synchronous segments in the 220–300 min and 320–400 min time interval. Amplitude signals from multiple channels are shown over time, with green coloured regions indicating time windows classified as synchronous events, and red regions indicating non-synchronous segments. Synchrony was evaluated pairwise across all 10 possible channel combinations (from 5 channels), and a window was classified as synchronous (green) if at least 7 of these 10 comparisons showed similar amplitude (within 0.018 units) and similar frequency (with a tolerance of 1 peak). The plot shows that synchronous events are characterized by lower frequencies and longer durations. Notably, from minute 360 onwards, the behaviour becomes predominantly asynchronous, with only brief and sporadic synchronous windows interrupting the overall pattern. (For interpretation of the references to colour in this figure legend, the reader is referred to the web version of this article.)

confirming the numerical findings.

Fig. 10 provides a detailed visualization of amplitude signals from multiple channels over time, with green-shaded regions indicating synchronous events and red regions corresponding to non-synchronous segments. Synchronous windows are characterized by lower amplitude and higher frequency, consistent with the statistical trends. Notably, from approximately 360 min onwards, the system transitions to a predominantly asynchronous regime with only brief, sporadic synchronous episodes interrupting the overall pattern. Table 1 summarizes the key statistical descriptors of synchronous and non-synchronous segments across the entire 83–1167 min interval. Together, these results indicate that synchronous states correspond to temporally stable, high-frequency configurations where multiple channels act coherently. This behaviour supports the hypothesis that electrical synchronicity reflects underlying collective processes of molecular reorganization within the peptide network, providing a direct link between microscopic aggregation dynamics and macroscopic electrical response.

In summary, the observed synchronicity reflects the emergence of cooperative molecular dynamics within the peptide network, suggesting that electrical coherence may serve as a macroscopic signature of microscopic reorganization events.

4. Simultaneous DLS and electrical measurements

To investigate the role of peptide spherule aggregation in the emergence of spontaneous electrical oscillations, we fabricated a 3D-printed support (using an Ultimaker S7) enabling the simultaneous acquisition of size distribution and electrical oscillations from the same MPA dispersion (Fig. 11). The setup was designed to host both a fibre-optic DLS (NanotracFlex, Verder Scientific) probe and a pair of passive platinum electrodes (Spe Medical) in the same reaction vessel. The DLS measurements were performed using a DLS probe allowing the real-time, non-invasive tracking of particle size and polydispersity directly in dispersion. The inline probe was positioned vertically above a

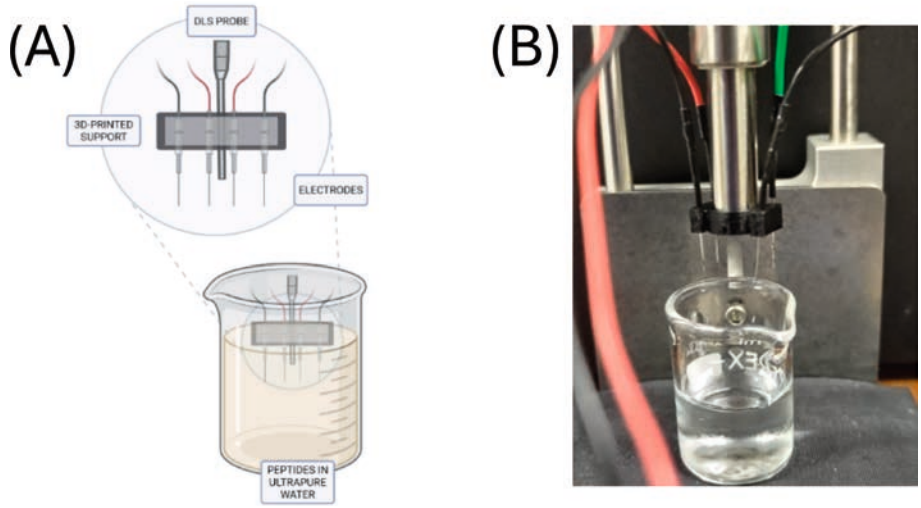


Fig. 11. (A) The 3D-printed experimental setup, combining a fiber-optic DLS probe and passive platinum electrodes immersed in the same peptide dispersion. The system enables simultaneous acquisition of real-time aggregation dynamics and spontaneous electrical activity of the MPA dispersion. Panel (B) reports a picture of the as-sketched setup.

Table 2

DLS Parameter	Signal feature	State	ρ	p-value	n
CS	amplitude_ch3	Asynchronous	−0.881	0.004	8
Mean number diameter	amplitude_ch3	Asynchronous	0.810	0.015	8
SD	amplitude_ch3	Asynchronous	0.762	0.028	8
CS	amplitude_ch3	Synchronous	−0.886	0.019	6
SD	amplitude_ch3	Synchronous	0.886	0.019	6
Mean number diameter	amplitude_ch3	Synchronous	0.771	0.072	6

standard borosilicate glass beaker containing the peptide aqueous dispersion, ensuring stable alignment and optimal signal quality. Passive electrodes were immersed in the same fluid volume, allowing for the detection of spontaneous electrical activity simultaneously with DLS monitoring. By synchronizing the DLS time series with electrical recordings, we were able to correlate synchronized phases of MPA oscillations with the dynamic evolution of the hydrodynamic diameter. Preliminary results indicate a statistical relationship between the aggregation state fluctuations and the oscillatory electrical signals. This integrated approach, hence offers a methodology to explore the biophysical basis of self-organized electrical activity in peptide-based soft matter systems.

To quantitatively assess the relationships between proteinoid aggregation dynamics and emergent electrical patterns, we employed a robust statistical framework combining non-parametric Spearman correlation with bootstrap resampling ($n = 1000$) to address the challenges of limited sample sizes and potential non-normal distributions inherent in exploratory biophysical studies. The analysis utilized 10 DLS measurement runs, with expanded temporal sampling yielding 15 total segments (7 synchronous, 8 asynchronous) through multi-segment association to enhance statistical power. Spearman's rank correlation was selected for its robustness to outliers and non-linear relationships, particularly valuable when the functional form of biophysical relationships remains unknown. The bootstrap procedure provided confidence intervals for correlation coefficients, offering crucial estimation uncertainty measures given the limited data points. This approach aligns with contemporary statistical practice for small-sample biological data, where traditional parametric assumptions may not hold. The significance threshold was maintained at $\alpha = 0.05$, while correlations with $|\rho| > 0.7$ were considered strong based on established conventions for biological correlation strength.

The analysis specifically focused on amplitude characteristics rather than frequency parameters, as preliminary investigation revealed limited variability in frequency measurements across segments. This decision enhanced the statistical power to detect meaningful relationships between DLS parameters (Mean_number_diameter, CS, SD, PDI, Mz, si) and signal amplitude features across individual channels and their aggregates.

In the following Table 2 are reported the statistically significant correlations between DLS aggregation parameters and electrical signal amplitudes. Correlation coefficients (ρ) represent Spearman rank correlations with associated p-values and sample sizes (n). The analysis reveals robust relationships between hydrodynamic size parameters (CS, Mean_number_diameter, SD) and amplitude characteristics of channel 3 signals across both synchronous and asynchronous states, highlighting the connection between proteinoid aggregation dynamics and emergent electrical pattern formation. The consistent correlation patterns across multiple DLS parameters reflect the intrinsic interdependence of size distribution metrics. Rather than indicating statistical redundancy, this coherence strengthens the biological interpretation that synchronized electrical activity in channel 3 is systematically related to the global particle size distribution profile. Note: The coherent correlation patterns across size parameters (CS, SD) reflect their intrinsic relationship in describing particle distribution characteristics. Channel 3 emerges as particularly sensitive to size distribution properties during synchronous states.

Fig. 12 illustrates the temporal correlation between the recorded electrical signal (bottom) and the hydrodynamic size measured via Dynamic Light Scattering (DLS, top). A clear modulation of the DLS response is observed depending on the synchronization phases of the electrical activity. During the synchronous phases of the electrical signal, characterized by regular and coordinated activity, a higher DLS value is recorded, indicative of a more aggregated state. This suggests a more organized and cooperative configuration of the system. Conversely, during the asynchronous phases, where the electrical signal appears more disordered or irregular, the system displays a lower DLS signal, corresponding to a more disaggregated or dispersed state. A specific temporal window was identified in which this dynamic modulation between synchronous and asynchronous phases, and the associated aggregation states, is particularly evident.

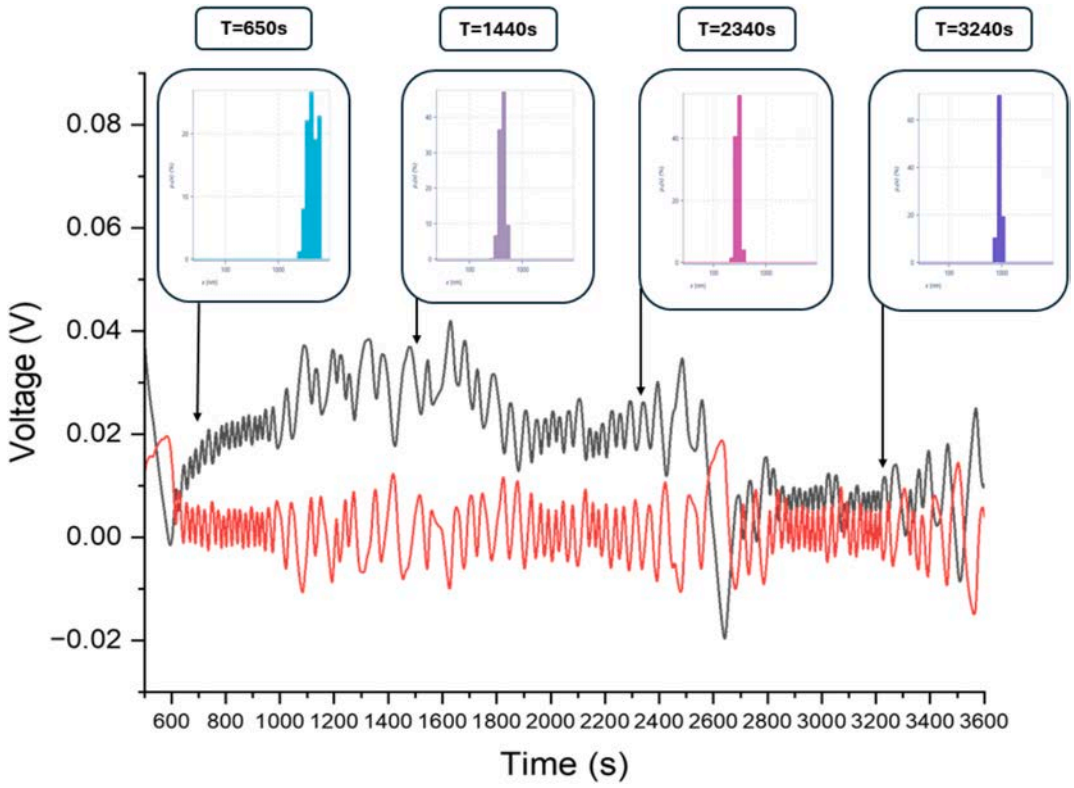


Fig. 12. Temporal correlation between electrical signal and hydrodynamic size measured by Dynamic Light Scattering (DLS). The bottom trace shows the electrical signal over time, while the top trace reports the corresponding DLS signal. Periods of synchronous electrical activity are associated with increased DLS values, indicating a more aggregated state. In contrast, asynchronous electrical phases correspond to reduced DLS signals, suggestive of a more disaggregated configuration.

5. PatchTST model for peptide spiking data

In this section, a mathematical model of MPA oscillation is proposed. In 2022, one of the co-authors of this paper [23], stated that the physical model for fluids, described by the Navier-Stokes equations, is not *generally solvable*[1] mathematically. The new prevailing thoughts are that one could frame this problem as a decision problem and work backwards and attempt to see whether certain formulations of the Navier-Stokes equations are Turing-machine computable [24], originally inspired by Tao [25]. One of the co-authors suggested, in the context of soft materials (such as gels, polymers, non-Newtonian fluids, and other complex fluids), that modern computing architectures, such as neural networks, might help in modelling their behaviour [26]. This idea recalls the way analogue computers once used modified flip-flop circuits at their core to simulate dynamic systems.[2] Recently, the authors of the current article extended the analogue computing argument presented above to the case of charged fluids [27], primarily because the mathematical pathologies in the Navier-Stokes equations (of not having a general solvability property) are fundamentally also present in the case of charged fluids (modelled using the Navier–Stokes–Nernst–Planck equations). In fact, in a recent work, [28] it, was shown that feedforward neural network architecture can capture temporal, statistical, and spectral features, in a 16-dimensional vector space, to accurately classify the proteinoid (binary) spiking time-series data, albeit with only 70.41% accuracy. In the current work, we use a much better, off-the-shelf model – PatchTST – which is suited to be trained on a (truncated) real-valued time-series data from a peptide system, thanks to its underlying transformer architecture. This goes without saying that some seminal works have adopted a material flow equilibration as the underlying process governing peptide self-organisation and electrical excitability, such as Matsuno in 1984 [16].

The next section will briefly discuss the modelling framework of PatchTST, followed by the details of implementation on the peptide dataset with the results thereafter, and broader applicability and generalisability of our approach to other possible scenarios.

5.1. PatchTST-based modelling framework for multivariate time-series forecasting

5.1.1. Problem setup

Let $\mathbf{x_t} \in \mathbb{R}^{\mathbf{M}}$ denote the M-dimensional observation at (discrete) time index t. Given a look-back window of length L, $(\mathbf{x_1}, \ldots, \mathbf{x_L})$, the forecasting task is:

$$(\mathbf{x_\{L+1\}}, \cdots, \mathbf{x_\{L+T\}}) = \mathscr{F}(\mathbf{x_1} \cdots \mathbf{x_L}) \tag{1}$$

where $\mathscr{F}(\cdot)$ is a learnable mapping parameterised by the PatchTST model.

5.1.2. Channel-wise patching

Following [21], each univariate slice (channel) $\mathbf{x^{(i)}} = (\mathbf{x_1^{(i)}}, \ldots, \mathbf{x_L^{(i)}}) \in \mathbb{R}^{\mathbf{1}} \times \mathbf{L}$, $i = 1, \ldots, M$, is split into *non-overlapping* or *partially overlapping* 1-D patches of length P with stride S. The resulting patch sequence is:

$$\mathbf{x_p^{(i)}} = [\mathbf{p_1^{(i)}}, \ldots, \mathbf{p_N^{(i)}}] \in \mathbb{R}^{\mathbf{P}} \times \mathbf{N}, \ \mathbf{N} = [(\mathbf{L} - \mathbf{P}) / \mathbf{S}] + \mathbf{2}, \tag{2}$$

where the final two patches hold a repeat of the last value to guarantee a fixed-length input.

[1] It is not known for a much wider class of smooth initial velocity fields, if the Navier–Stokes equations, after certain finite time, yield a smooth solution – (a) which blows up or (b) remains regular.

[2] Notably, Tao used a sequence of quadratic circuits connected in series to simulate non-linear inter-actions inherent in a system of ODEs (variant to dyadic shell model) with the (Euler bilinear operator) as a carefully selected averaged version of the one for the Navier-Stokes equations.

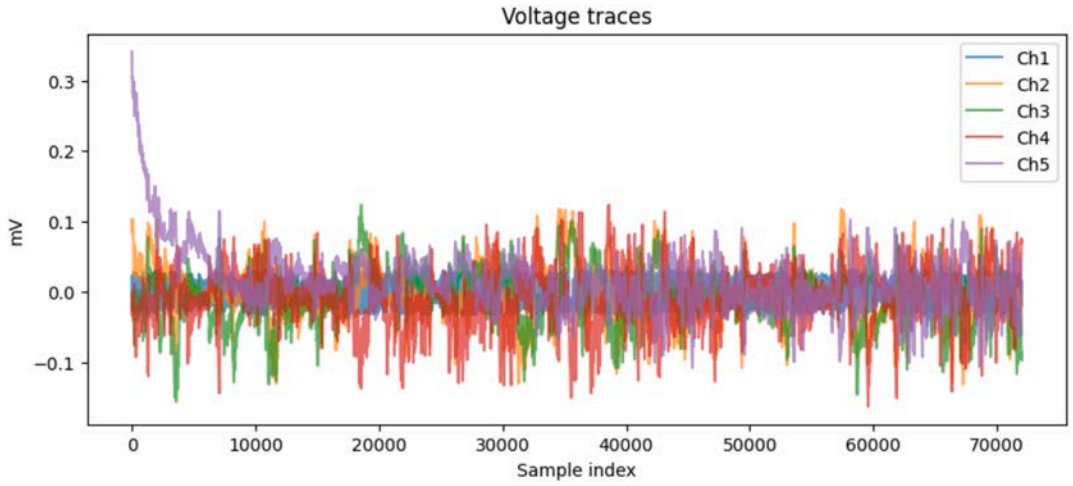


Fig. 13. Raw voltage traces recorded from five channels (Ch1–Ch5) over time. The traces are plotted against the sample index to visualize baseline fluctuations and channel variability in the signal.

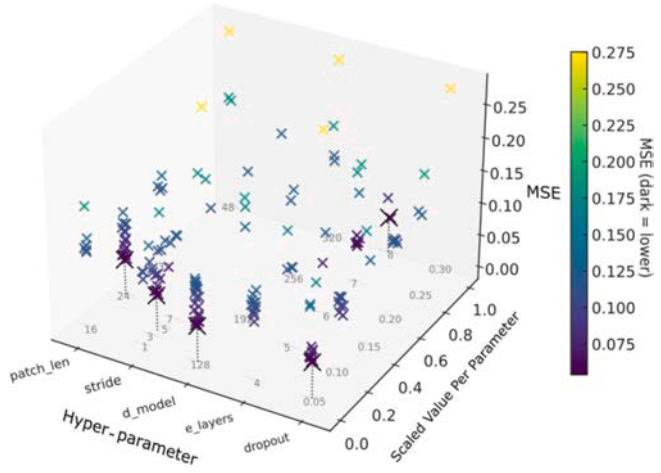


Fig. 14. Three–dimensional point-cloud of PatchTST hyper-parameter searches. The five vertical "curtains" correspond to the five tuned hyper-parameters – patch len, stride, d model, e layers, and dropout – each scaled individually to the range [0,1] on the y-axis, with their raw values annotated on the base plane (z = 0). Every dot represents one Optuna trial; its height and colour encode the resulting mean-squared error (MSE), with dark-violet indicating lower error and yellow indicating higher error. The globally best trial is emphasised by a larger cross mark, and dotted guidelines project this optimum down to its exact hyper-parameter settings (24,4,128,8,0.05) on the base plane. Where $\mathcal{F}(\cdot)$ is a learnable mapping parameterised by the PatchTST model. (For interpretation of the references to colour in this figure legend, the reader is referred to the web version of this article.)

5.1.3. Transformer encoding

Each patch is linearly projected to a *D*-dimensional latent:

$$\mathbf{e_j^{(i)}} = \mathbf{W_p \cdot p_j^{(i)}} + \mathbf{W_s \cdot \ell_j}$$

where $\mathbf{W_p} \in \mathbb{R}^{\mathbf{D}\times\mathbf{P}}$, $\mathbf{W_s} \in \mathbb{R}^{\mathbf{D}\times\mathbf{P}}$, and $\boldsymbol{\ell}_\mathbf{j}$ is a learnable positional code.

Stacking the *N* embeddings gives:

$$\mathbf{E^{(i)}} = \mathbf{[e_1^{(i)}, \ldots, e_N^{(i)}]} \in \mathbb{R}^{\mathbf{D}\times\mathbf{N}}$$

which is fed into a Vanilla multi-head Transformer encoder:

$$\mathbf{Q_h^{(i)} = (W_h \hat{} Q \cdot E^{(i)})^T},\ \mathbf{K_h^{(i)} = (W_h \hat{} K \cdot E^{(i)})^T},\ \mathbf{V_h^{(i)} = (W_h \hat{} V \cdot E^{(i)})^T},\ \mathbf{O_h^{(i)}} = \mathbf{softmax((Q_h^{(i)} \cdot (K_h^{(i)})^T) / \sqrt{d_k})\ V_h^{(i)}}, \quad (3)$$

with usual residual, layer-norm, and feed-forward blocks; $\mathbf{z^{(i)}} \in \mathbb{R}^{\mathbf{D}\times\mathbf{N}}$ denotes the output sequence representation.

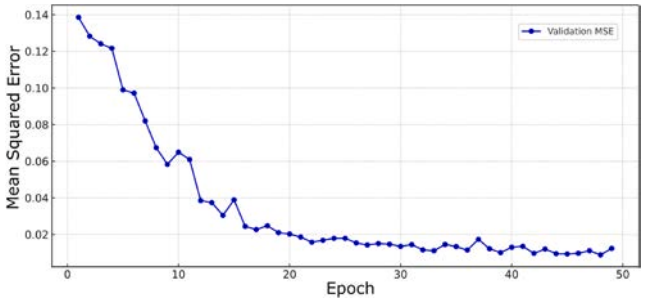


Fig. 15. Validation MSE across 50 training epochs. The error steadily declines, reaching a minimum around epoch 49.

5.1.4. Forecast head and loss

A flatten-then-linear layer maps $\mathbf{z^{(i)}}$ to the forecast $\mathbf{x\hat{}^{(i)}\{L+1:L+T\}} \in \mathbb{R}^{\mathbf{1}} \times \mathbf{T}$. We minimise channel-wise mean-square error (MSE):

$$\mathscr{L} = \mathbf{(1/M)} \cdot \sum_{\mathbf{(i=1)}}\hat{}\mathbf{M} \left\|\mathbf{x\hat{}^{(i)}\{L+1:L+T\} - x^{(i)}\{L+1:L+T\}}\right\|_2^2, \quad (4)$$

5.1.5. Flip-flop complexity analysis

For a sequence length **L**, a baseline Transformer incurs $\mathscr{O}(\mathbf{L^2})$ attention cost. With patching, the token count is reduced to $\mathbf{N} \approx \mathbf{L/S}$ (cf. Eq. (2)), giving

$$\mathscr{O}\left(\mathbf{N^2}\right) = \mathscr{O}\left(\mathbf{(L/S)^2}\right) = \mathscr{O}\left(\mathbf{L^2/S^2}\right), \quad (5)$$

i.e. *quadratically smaller by a factor* S^2. A promising direction is to replace soft-attention with AFNO [23] (spectral mixing), which scales as $\mathscr{O}$(N log N); combining AFNO with patching conjecturally implies an overall cost $\mathscr{O}$((L/S) log (L/S)).

5.1.6. Results

We evaluated the performance of the PatchTST model on multivariate time-series data collected across five electrophysiological channels (Ch1–Ch5). The raw voltage traces, shown in Fig. 13, exhibit heterogeneous baseline fluctuations and varying channel noise characteristics, underscoring the need for robust modeling strategies.

To optimise the model, we performed an extensive Optuna hyper-parameter sweep across key dimensions: **patch_len**, **stride**, **d_model**,

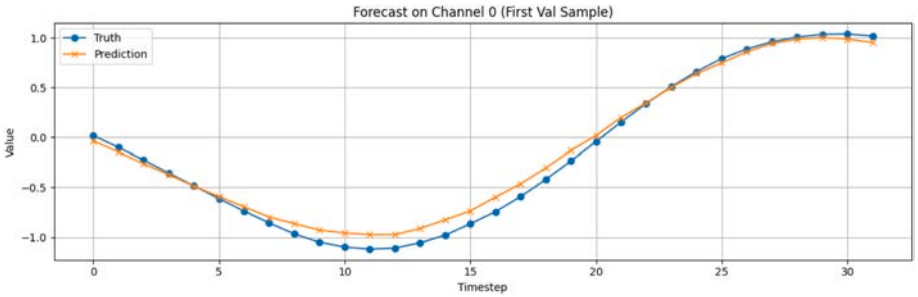


Fig. 16. Forecasted signal (orange) versus ground truth (blue) on Channel 1 for a validation sample. The model captures both the phase and amplitude of the time-series data with minimal deviation across timesteps. (For interpretation of the references to colour in this figure legend, the reader is referred to the web version of this article.)

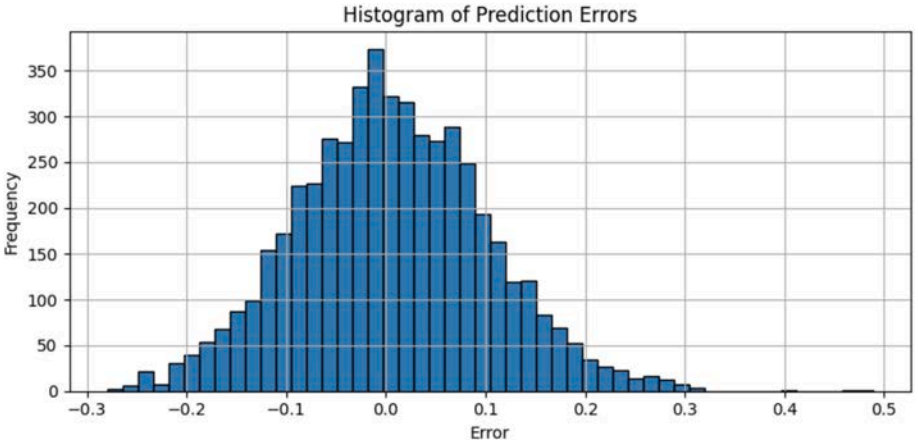


Fig. 17. Histogram of prediction errors across the test set. The distribution is centered around zero, suggesting the model has low bias and symmetric prediction error characteristics.

e_layers, and **dropout**. The 3D scatter plot in Fig. 14 illustrates the distribution of trials with respect to mean squared error (MSE). Lower MSE values are visually encoded by darker hues and higher point elevations. The optimal configuration found was: **patch_len = 24, stride = 4, d_model = 128, e_layers = 8, dropout = 0.05**.

Using the best hyperparameters, we trained the model for 50 epochs. Fig. 15 compares the model's forecast (orange) against the ground truth (blue) for one validation sample from Channel 1. The prediction closely follows the true signal trajectory, successfully capturing both the phase and amplitude. The final performance on the validation set achieved an MSE = 0.000934, MAE = 0.07637, and R2 score = 0.99087. The model's learning progression is shown in Fig. 16, where MSE is plotted across training epochs. The error consistently reduces, stabilizing around Epoch 49, suggesting convergence without overfitting. Fig. 17 shows the histogram of prediction errors for the test set. The error distribution is tight and centered around zero, indicating low bias. The narrow spread and symmetric shape also suggest low variance, consistent generalization, and the absence of both under- and over-fitting.

Broader Applicability. Because patching disentangles local from global dependencies, the framework extends cleanly to ultra-high-frequency market-making streams (e.g., limit-order-book snapshots). Near-real-time inference remains feasible thanks to the $\mathcal{O}(L^2/S^2)$ complexity we derived in Eq. (5), even when L covers thousands of ticks.

Code. The GitHub version of the Colab notebook is available here.

6. Conclusion and perspective

This study investigates a minimal peptide-based material obtained through abiotic, non-enzymatic thermal polymerization of amino acids, with the aim of elucidating the material-level origin of its spontaneous oscillatory electrical behaviour. Multimodal chemical, structural, and morphological characterization shows that the system consists of a chemically heterogeneous ensemble of short peptide oligomers forming dynamic aggregates in aqueous environments. Electrical measurements reveal reproducible autonomous oscillatory signals arising under constant environmental conditions. Importantly, the use of simultaneous dynamic light scattering and electrical measurements establishes a direct correlation between aggregation-disaggregation dynamics and electrical oscillations. This structure–function coupling supports the interpretation of the electrical activity as an emergent collective property of the material, rather than as a molecular feature of individual peptide species. Control experiments confirm that this behaviour is intrinsic to the peptide material and not an artefact of the experimental setup. From a materials design perspective, these results demonstrate how intrinsic electrical functionality can emerge from chemically heterogeneous peptide ensembles through simple processing routes and collective organization. The work provides experimentally grounded insight into processing-structure–property relationships in peptide-based systems and identifies minimal peptide assemblies as a functional materials platform in which dynamic aggregation can be exploited to generate non-trivial electrical behaviour. These findings are relevant to the development and interpretation of peptide-based functional materials, with potential implications for peptide electronics and unconventional computing architectures.

CRediT authorship contribution statement

Salvatore Del Basso: Writing – original draft, Visualization, Methodology, Investigation, Formal analysis, Data curation. **Pietro Squeri:** Methodology, Investigation, Formal analysis, Data curation, Software,

Validation, Visualization, Writing – original draft. **Rishit Mohan Ahuja:** . **Rishav Karki:** Data curation, Formal analysis, Software, Visualization. **Giuseppe De Giorgio:** Methodology, Investigation. **Vardan Galstyan:** Methodology, Investigation, Writing – review & editing. **Raffaele Martucci Zecca:** Methodology, Formal analysis, Investigation, Visualization. **Enrico Dalcanale:** Methodology, Formal analysis, Validation, Writing – review & editing, Data curation. **Xiongchuan Huang:** Validation, Investigation, Methodology, Writing – review & editing. **Davide Vurro:** Validation, Methodology, Formal analysis, Investigation, Writing – review & editing. **Saksham Sharma:** Writing – review & editing, Validation, Methodology, Data curation, Formal analysis, Investigation. **Pasquale D'Angelo:** Writing – review & editing, Supervision, Methodology, Funding acquisition, Validation, Writing – original draft. **Andrew Adamatzky:** Writing – review & editing, Validation, Conceptualization, Investigation, Methodology, Supervision. **Giuseppe Tarabella:** Writing – original draft, Visualization, Supervision, Methodology, Funding acquisition, Conceptualization, Investigation, Writing – review & editing.

Funding

This work was supported by the Italian Ministry of Foreign Affairs and International Cooperation (MAECI) grant number CN24GR09 (CUP B53C24001100001). GT, PD, VG acknowledge the National Recovery and Resilience Plan (NRRP), Mission 04 Component 2 Investment 1.5 – NextGenerationEU, Award Number: 0001052 dated June 23, 2022. GT, PD, DV acknowledge the support by the European EIC Pathfinder Challenger project (project number: 101115545): In-Vessel implantable smart sensing device for personalized medicine (IV-Lab).

Declaration of competing interest

The authors declare that they have no known competing financial interests or personal relationships that could have appeared to influence the work reported in this paper.

Acknowledgment

We acknowledge the Interdepartmental Centre Measures (CIM) of the University of Parma for providing access to NMR and HPLC facilities. G.T., P.D. and S.D.B. gratefully acknowledge Dr. Giacomo Quilici for his valuable support and collaboration in the acquisition and analysis of the NMR data.

Data availability

Data will be made available on request.

References

[1] S.D. Fried, K. Fujishima, M. Makarov, I. Cherepashuk, K. Hlouchova, Peptides before and during the nucleotide world: an origins story emphasizing cooperation between proteins and nucleic acids, J. R. Soc. Interf. 19 (187) (2022), https://doi.org/10.1098/RSIF.2021.0641; JOURNAL:JOURNAL:RSIF;REQUESTEDJOURNAL:JOURNAL:RSIF;PAGE:STRING:ARTICLE/CHAPTER.

[2] A. Adamatzky, Towards proteinoid computers. Hypothesis paper, Biosystems 208 (2021) 104480, https://doi.org/10.1016/J.BIOSYSTEMS.2021.104480.

[3] P. Mougkogiannis, A. Adamatzky, Electrical properties of proteinoids for unconventional computing architectures, ACM Int. Conf. Proc. Ser. (2023), https://doi.org/10.1145/3611315.3633264/ASSETS/HTML/IMAGES/NANOARCH23-29-FIG4.JPG.

[4] P. Mougkogiannis, A. Adamatzky, Learning in ensembles of proteinoid microspheres, Jun. 2023, http://arxiv.org/abs/2306.14362 (Accessed: Aug. 03, 2025).

[5] P. Mougkogiannis, A. Adamatzky, Proteinoid microspheres as protoneural networks, ACS Omega 8 (38) (2023) 35417–35426, https://doi.org/10.1021/ACSOMEGA.3C05670/ASSET/IMAGES/LARGE/AO3C05670_0009.JPEG.

[6] Peptide Materials, *Biomacromolecules* 24(26) (2025) 4051–4063, doi: 10.1021/acs.biomac.3c00422.

[7] L. Yuan and L. Liu, Peptide-Based Electrochemical Biosensing, Oct. 01, 2021, *Elsevier B.V.* doi: 10.1016/j.snb.2021.130232.

[8] J. G. Zhao, J. Cao, and W. Z. Wang, Peptide-based electrochemical biosensors and their applications in disease detection, Jun. 01, 2022, *Nonferrous Metals Society of China*. doi: 10.1007/s41664-022-00226-y.

[9] S.W. Fox, T. Nakashima, The assembly and properties of protobiological structures: the beginnings of cellular peptide synthesis, Biosystems 12 (3–4) (1980) 155–166, https://doi.org/10.1016/0303-2647(80)90013-1.

[10] Y. Ishima, A.T. Przybylski, S.W. Fox, Electrical membrane phenomena in spherules from proteinoid and Lecithin, Biosystems 13 (4) (1981) 243–251, https://doi.org/10.1016/0303-2647(81)90004-6.

[11] A.T. Przybylski, S.W. Fox, Excitable artificial cells of proteinoid, Appl. Biochem. Biotechnol. 10 (1) (1984) 301–307, https://doi.org/10.1007/BF02783764.

[12] P. Mougkogiannis, A. Adamatzky, Light induced spiking of proteinoids, Biosystems 232 (2023), https://doi.org/10.1016/j.biosystems.2023.105015.

[13] P. Mougkogiannis, N. Phillips, A. Adamatzky, Transfer functions of proteinoid microspheres, Biosystems 227–228 (2023), https://doi.org/10.1016/j.biosystems.2023.104892.

[14] R. Xing, C. Yuan, W. Fan, X. Ren, X. Yan, Biomolecular glass with amino acid and peptide nanoarchitectonics, Sci. Adv. 9 (11) (2023), https://doi.org/10.1126/SCIADV.ADD8105; PAGE:STRING:ARTICLE/CHAPTER.

[15] C. Yuan, W. Fan, P. Zhou, R. Xing, S. Cao, X. Yan, High-entropy non-covalent cyclic peptide glass, Nat. Nanotechnol. 19 (12) (2024) 1840–1848, https://doi.org/10.1038/s41565-024-01766-3.

[16] K. Matsuno, Electrical excitability of proteinoid microspheres composed of basic and acidic proteinoids, Biosystems 17 (1) (1984) 11–14, https://doi.org/10.1016/0303-2647(84)90011-X.

[17] Y.P. Gunji, A. Adamatzky, Computation implemented by the interaction of chemical reaction, clustering, and de-clustering of molecules, Biomimetics 9 (7) (2024) 432, https://doi.org/10.3390/BIOMIMETICS9070432.

[18] P.I. Haris, D. Chapman, The conformational analysis of peptides using fourier transform IR spectroscopy, Biopolymers 37 (4) (1995) 251–263, https://doi.org/10.1002/BIP.360370404;PAGE:STRING:ARTICLE/CHAPTER.

[19] J.S. Cobb, V. Zai-Rose, J.J. Correia, A.V. Janorkar, FT-IR spectroscopic analysis of the secondary structures present during the desiccation induced aggregation of elastin-like polypeptide on silica, ACS Omega 5 (14) (2020) 8403–8413, https://doi.org/10.1021/ACSOMEGA.0C00271/ASSET/IMAGES/LARGE/AO0C00271_0003.JPEG.

[20] C. R. Harris et al., Array programming with NumPy, Sep. 17, 2020, Nature Research. doi: 10.1038/s41586-020-2649-2.

[21] J.D. Hunter, Matplotlib: a 2D graphics environment, Comput. Sci. Eng. 9 (03) (2007) 90–95, https://doi.org/10.1109/MCSE.2007.55.

[22] P. Virtanen, et al., SciPy 1.0: fundamental algorithms for scientific computing in Python, Nat. Methods 17 (3) (2020) 261–272, https://doi.org/10.1038/s41592-019-0686-2.

[23] S. Sharma, G. Marcucci, A. Mahmud, A complexity perspective on fluid mechanics, Nov. 2022, Accessed: Jul. 26, 2025. [Online]. https://arxiv.org/pdf/2212.00153.

[24] R. Cardona, E. Miranda, D. Peralta-Salas, F. Presas, Constructing turing complete Euler flows in dimension 3, Proc. Natl. Acad. Sci. U.S.A. 118 (19) (2021), 10.1073/PNAS.2026818118;PAGE:STRING:ARTICLE/CHAPTER.

[25] T. Tao, Finite time blowup for an averaged three-dimensional Navier-Stokes equation, J. Am. Math. Soc. 29 (3) (2016) 601–674, https://doi.org/10.1090/JAMS/838.

[26] S. Sharma, G. Marcucci, From Navier-Stokes millennium-prize problem to soft matter computing, PNAS Nexus, pp. 1–9, 2022, [Online]. Available: https://arxiv.org/pdf/2212.01492 (Accessed: Jul. 26, 2025).

[27] G. De Giorgio, G. Tarabella, Pasquale D'angelo, S. Sharma, Advances in Prebiotic Chemistry: The Potential of Analog Computing and Navier-Stokes-Nernst-Planck (NPNS) Modeling in Organic Electrochemical Transistors (OECTs), *BioNanoScience* 15(3) (2025) 1–9, doi: 10.1007/S12668-025-02068-1.

[28] S. Sharma, A. Mahmud, G. Tarabella, P. Mougoyannis, A. Adamatzky, Graph-based Complexity and Computational Capabilites of Proteinoid Spike Systems, Apr. 2025, Accessed: Jul. 26, 2025. [Online]. Available: https://arxiv.org/pdf/2504.10362.